Rectification effects of regional air–sea interactions over western boundary current on large-scale sea surface temperature and extra-tropical storm tracks

Lionel Renault, Thomas Arsouze, Fabien Desbiolles, Justin Small

scientific reports

Check for updates

OPEN

Rectification effects of regional air–sea interactions over western boundary current on large-scale sea surface temperature and extra-tropical storm tracks

Lionel Renault[1]✉, Thomas Arsouze[2,3,4], Fabien Desbiolles[1,5,6] & Justin Small[7]

The warm Western Boundary Currents (WBCs) and their zonal extensions are persistent, deep, strong and narrow oceanic currents. They are known to anchor and energize the Extra-Tropical storm tracks by frontal thermal air–sea interactions. However, even in the latest generation of climate models, WBCs are characterized by large biases, and both the present storm-track activity and its recent intensification are poorly estimated. Mesoscale air–sea interactions, and in particular the Current Feedback to the Atmosphere (CFB) have been shown to be important in ocean and in particular WBC dynamics as they modify the energy budget of the ocean. CFB causes eddy-killing by drag friction between currents and the atmosphere. It damps the oceanic eddy activity, and, thus, weakens the eddy-mean flow interaction, stabilizing WBCs. Based on cutting-edge high-resolution coupled global simulations, we show that the stabilization of WBCs by CFB modulates the mean Sea Surface Temperature and its meridional gradients as well and the turbulent heat fluxes between the ocean and the atmosphere. This alters the baroclinicity of the lower atmosphere, which in turn modulates the extra tropical storm-tracks intensity by up to 15%.

Extra-tropical warm Western Boundary Currents (WBCs), the Gulf Stream, the Kuroshio, and the Agulhas Current and their zonal extensions are persistent, deep, and narrow currents and are among the strongest oceanic currents on Earth. Progressively, they have been recognized as major emblematic oceanic features that shape the Earth's climate[1–5]. Extra-tropical cyclones occur partly over the same region, *i.e.*, within the so-called extra-tropical storm-tracks, located in the 30–60°latitude band[2,6–8]. They are of tremendous importance for global climate. They advect energy poleward, mitigating the energy imbalance between the Equator and the Poles[6,9]. They also modulate winds, temperature, humidity, and precipitation on daily to multidecadal timescales[10–12]. However, the representation of both WBCs and extra-tropical storm tracks in climate models, and especially in climate change projections, is subject to large uncertainties, and a better understanding of the underlying dynamics is needed to reduce them[13–15].

Several factors have an influence on the extra-tropical storm tracks, such as land topography, land–sea boundaries and Sea Surface Temperature (SST) patterns[10,16,17]. Fundamentally, cyclone development is strongly related to baroclinic instability in the lower troposphere[18–21], which is maintained in particular over WBCs by two main mechanisms[3–5,16,22–24]. On the one hand, WBCs transport considerable amounts of heat from the subtropical oceans into the mid-latitudes[1]. This induces large-scale meridional SST gradients, which sustain meridional air temperature gradients in the lower troposphere, and, thus, the baroclinicity of the lower atmosphere. These atmospheric gradients tend to be counterbalanced by poleward transient eddy heat fluxes[21,25,26], but are restored by the SST gradients[26,27]. On the other hand, as WBCs separate from the coastal boundaries and zonally extend into the ocean interior, they are prone to the largest transfer of heat from the ocean to the atmosphere over the global ocean (more than 200 W m^{-2})[2,3,28,29]. This heat loss can also alter the

[1]LEGOS, University of Toulouse, IRD, CNRS, CNES, UPS, Toulouse, France. [2]Barcelona Supercomputing Center, Barcelona, Spain. [3]CIRAD, UMR AMAP, 34398 Montpellier, France. [4]AMAP, Univ Montpellier, CIRAD, CNRS, INRAE, IRD, Montpellier, France. [5]Department of Earth and Environmental Sciences, Università di Milano-Bicocca, Milan, Italy. [6]CIMA Research Foundation, 17100 Savona, Italy. [7]Climate and Global Dynamics Laboratory, NSF National Center for Atmospheric Research, 1850 Table Mesa Drive, Boulder, CO 80305, USA. ✉email: lionel.renault@ird.fr

static stability of the lower atmosphere, increasing the baroclinicity of the lower atmosphere[7,8,30–32]. In winter, the heat loss by WBCs can be enhanced by both outbreaks of dry and cold air from the continent[33–35].

In the past decades, thanks to satellite data and high-resolution climate simulations, air-sea interactions at the oceanic mesoscale (*i.e.,* scales of 10–100 km and 10–100 days, *e.g.,* [36,37]) have received a growing interest from the scientific community. Several studies have shown that ocean eddies and fronts have a major influence on the ocean and atmosphere through mesoscale air-sea interactions (see[38] and[24] for a review). So far, two main mesoscale air-sea interactions have been assessed: the Thermal FeedBack (TFB) and Current FeedBack (CFB).

TFB is essentially the influence of SST and SST gradients on the overlying atmosphere. It alters the turbulent exchange of heat between the ocean and the atmosphere (latent and sensible heat), the atmospheric pressure gradients, the stability of the atmospheric boundary layer, and other atmospheric processes (see[38] and[24] for reviews). Turbulent heat fluxes anomalies caused by oceanic mesoscale eddies are often between 20 and 50 W m^{-2} C^{-1}[39,40]. They damp the SST signature of the eddies[41] and can be understood in terms of a sink of eddy potential energy to the atmosphere[42]. Changes in vertical mixing of momentum, pressure adjustment, and atmospheric boundary layer stability, result in surface wind speed anomalies that are generally positive over warm SSTs and negative over cold SSTs. The wind anomalies cause Ekman vertical velocities in the ocean, but generally do not modulate the mesoscale energy budget of the ocean[43]. While the influence of TFB on storm tracks has been extensively studied (*e.g.,* [3–5,22–25,44]), the effects of CFB are less understood.

CFB expresses the influence of surface ocean currents on the overlying atmosphere. It acts mainly through changes in surface stress. In a coupled model, CFB is accounted for by estimating the surface stress using the relative wind to the ocean currents (see[45] for its practical implementation):

$$\boldsymbol{\tau} = \rho_a C_D(\boldsymbol{U}_a - \boldsymbol{U}_o)|\boldsymbol{U}_a - \boldsymbol{U}_o|, \tag{1}$$

where $\boldsymbol{\tau}$ is the surface stress, ρ_a is the density of the air, C_D is the drag coefficient, and $\boldsymbol{U}_a$ and $\boldsymbol{U}_o$ are the 10 m wind and the surface current, respectively. When neglecting the current feedback, the stress is estimated as

$$\boldsymbol{\tau}_a = \rho_a C_D \boldsymbol{U}_a|\boldsymbol{U}_a|. \tag{2}$$

The surface stress response to CFB is linearly related to the current vorticity: a negative vorticity yields a positive surface stress curl and vice versa[46,47]. The large-scale effect of CFB is a slow down of the mean oceanic circulation that is induced by a reduction in the mean energy input from the atmosphere to the ocean[48–51]. More importantly, at the mesoscale, CFB induces sinks of kinetic energy from the ocean to the atmosphere[50–53], *i.e.,* the so-called eddy killing, which damps the mesoscale activity by about 30% overall[54–60]. Oceanic eddy killing is the main CFB mechanism. By reducing the reservoir of mesoscale kinetic energy, CFB causes a weakening of the eddy-mean flow interaction (the inverse cascade of energy in the ocean): mesoscale eddies transfer less energy to large-scale currents such as WBCs, altering their mean positions and characteristics and stabilizing them[51,61–66].[67] and[64], using a regional ocean-atmosphere coupled model over a 5-year period, demonstrate that the CFB-induced stabilization of the Agulhas Current: it causes a greater advection of warm water from the Indian Ocean into the South Atlantic Ocean, which alters the mean SST and, subsequently the local precipitation. This modulates the turbulent heat fluxes and the mean SST gradients, altering the baroclinicity of the lower atmosphere, and, thus, the extra-tropical storm tracks over the South Indian Ocean[64].

In this study, we aim to extend the evaluation of the rectification effect of the mesoscale CFB on the extratropical storm track, focusing mainly on the Gulf Stream, the Kuroshio, and the Agulhas Current. Specifically, we aim to achieve the following three objectives:

1. Demonstrate on a global scale the mesoscale CFB effect, including the surface stress response and the eddy killing effect, which have mostly been assessed on a regional scale.
2. Evaluate the associated upscaling effect on the oceanic mean state, focusing on mean currents and SST;
3. Determine the rectification effect on extratropical storm tracks.To achieve these objectives, we take advantage of the cutting-edge coupled eddy-rich global ocean–atmosphere simulations carried out within the PRIMAVERA project (https://www.primavera-h2020.eu/) as part of HighResMIP[68]. We use the Very High Resolution "VHR" ORCA12 / IFS1279 configuration of the EC-Earth climate model[69–71], which has a spatial resolution of ≈ 7 km for the ocean and ≈ 15-km for the atmosphere (see "Methods"). Both spatial resolutions meet the requirements to properly simulate the extratropical storm tracks, as shown by[23], which is confirmed by the comparison of the extra-tropical storm tracks simulated by the "VHR" simulation and coarser climate model simulations in[71]. Two experiments are available: C_{CFB} considers both TFB and CFB, and C_{NOCFB} considers TFB but neglects CFB (see "Methods"). C_{NOCFB} is available for a period of 80 years and is the original PRIMAVERA simulation. C_{CFB} is available for a period of 24 years and was run specifically for this study. In the following, we use a bootstrap method[72] to disentangle the differences due to CFB from internal and climate variability. We consider the 80 years of the C_{NOCFB} simulation as our population data and compute 1000 samples on 24 unique and not necessarily consecutive years (see "Methods"). The 1000 samples of C_{NOCFB} are then compared to C_{CFB}.

Results

A partial control of the ocean dynamics by CFB

The main direct effect of CFB is to systematically induce surface stress curl anomalies that are anticorrelated with surface current vorticity (*e.g.,* [46]): positive surface current vorticity causes negative surface stress curl, and

vice versa. At the mesoscale, the strength of this coupling has been measured by the coupling coefficient s_τ, which is defined as the slope of the linear regression between mesoscale surface stress curl and mesoscale ocean current vorticity (see "Methods"). s_τ in a simulation without CFB (as C_{NOCFB}) is approximately zero[47,54]. In Fig. 1a, s_τ is estimated over the 24-year simulated period of C_{CFB}. s_τ in C_{CFB} is characterized by negative values everywhere and an intensity on the order of -10^{-2} N s m$^{-}3$, which is consistent with the values found in previous regional studies[47,54]. s_τ depends primarily on the wind strength[52,59]: the stronger the wind, the more negative the s_τ. Consistent with the literature, s_τ has its largest negative values within extratropical storm tracks and over the eastern boundary upwelling system.

The surface stress anomalies caused by CFB and measured with the s_τ coupling coefficient cause a transfer of kinetic energy from mesoscale eddies to the atmosphere, which can be expressed by the geostrophic eddy wind work (F_eK_{eg}, m^3s^{-3})[54]:

$$F_eK_{eg} = \frac{1}{\rho_0}\boldsymbol{u_g'\tau'}, \tag{3}$$

where prime denotes the eddy part of the signal estimated using a Gaussian spatial filter (see "Methods"), ρ_0 is the ocean surface density, $\boldsymbol{u_g}$ and $\boldsymbol{\tau}$ are the geostrophic currents and surface stress, respectively. Figure 1b shows F_eK_{eg} estimated from C_{CFB}. Consistent with previous studies (*e.g.,* [50,52,54,59,66]), F_eK_{eg} is negative almost everywhere, revealing the presence of the eddy killing mechanism, *i.e.,* a sink of kinetic energy from mesoscale oceanic currents to the atmosphere of -72.5 GW, which is consistent with previous estimates from observations[53,67,73]. At these scales, this implies that the ocean is forcing the atmosphere, rather than the classical view of an atmosphere forcing the ocean on a large scale, initiating a turbulent energy cascade. F_eK_{eg} is larger over the WBCs and the Antarctic Circumpolar Current. Some positive values are present near the coast and offshore. They correspond to regions where the mesoscale activity is weak and mostly composed of wind-driven currents[74]. The energy sinks can be partially observed from satellite data[52,73] and are absent in a simulation without CFB as C_{NOCFB}[54,58].

The surface Eddy Kinetic Energy (EKE) is estimated as a proxy for the oceanic mesoscale activity using the daily anomalies (with the same spatial filter as for F_eK_{eg}, see "Methods") of the surface geostrophic currents ($EKE = 0.5(u'^2 + v'^2)$). The mean pattern and intensity of the EKE in C_{CFB} are consistent with the

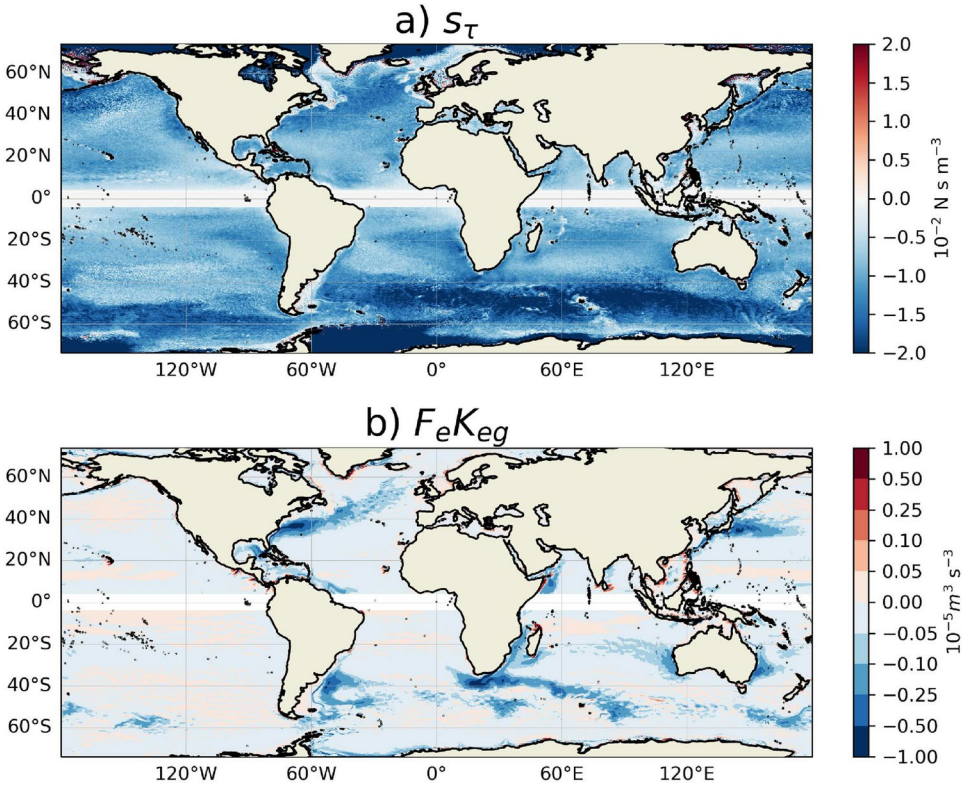

Fig. 1. The CFB induces a sink of kinetic energy from oceanic mesoscale eddies to the atmosphere, *aka* the eddy killing. (**a**) Coupling coefficient s_τ estimated from C_{CFB} (spatially smoothed over 50 km to diminish noise). s_τ can be interpreted as a proxy for the efficiency of the eddy killing. (**b**) Eddy windwork (F_eK_{eg}) estimated from C_{CFB}. The negative values reveal a transfer of kinetic energy from mesoscale currents to the atmosphere. The maps were generated using Python 3.0 (https://www.python.org/).

literature (see Supplemental Information). Figure 2a shows the difference between the EKE estimated from C_{CFB} and C_{NOCFB}. The sink of kinetic energy induced by CFB causes the oceanic eddy killing mechanism, *i.e.,* a damping of the EKE. On average, from C_{NOCFB} to C_{CFB}, the EKE is reduced by $\approx 30\%$. This improves the realism of the simulation and is in agreement with previous studies *e.g.,* [54,55,58,59], but here it is demonstrated on a global scale and over a long time period. The largest difference is, not surprisingly, located over the most eddying regions, such as WBCs, which is in agreement with *e.g.,* [59,62–64,67].

The reduction of the EKE leads to a weakening of the eddy-mean-flow interaction (the so-called inverse cascade of energy), which stabilizes and modifies the paths of the strongest oceanic currents, including the WBCs[51,57,61,62,66,75]. The changes in the WBC paths are associated with the dipole of the negative and positive EKE difference 2a. Figure 2b shows the difference of the mean kinetic energy between C_{CFB} and C_{NOCFB}. It confirms the stabilization of the WBC paths by the eddy killing mechanism and reveals the presence of a dipole above the WBCs. This improves the realism of the simulation (see Supplemental Information), especially above the WBCs, where the biases in C_{CFB} are reduced with respect to C_{NOCFB}. As shown in[51], the weakening of the eddy-mean flow interactions dominates the large-scale effect of CFB (*i.e.,* the slow down of the mean currents) on the WBCs. Finally, CFB also causes a reduction in the mean equatorial surface current, consistent with[49].

An upscaling effect on the mean SST and mean SST gradients

Figure 3a shows the difference in mean SST between C_{CFB} and C_{NOCFB}. The oceanic eddy killing caused by CFB has an upscaling effect on the SST. Over WBCs, the SST difference can reach up to 2°C, which is consistent with previous regional studies of[57,64]. Two different behaviors can be highlighted over the WBCs. Over the Gulf Stream and the Kuroshio, the CFB causes a warming (cooling) of the SST to the north (south) of the currents, consistent with changes in their mean paths. For the Agulhas Current, consistent with[57,64], the CFB causes a west-east dipole of warming/cooling over the Agulhas retroflection region and warming over its zonal extension. Other regions of the world ocean are affected to a lesser extent, such as the Southern Ocean, the equatorial regions of the Pacific, and the west coast of the USA, with SST differences up to 0.5°C. Finally, in the Arctic Ocean, there are substantial changes along the sea ice margins, which may be related to differences in water mass formation that can affect sea ice cover. In general, this rectification effect largely reduces the biases in the mean SST from C_{CFB} to C_{NOCFB}, especially over the WBCs (see Supplemental Information).

The changes in SST are associated with changes in the mean absolute meridional SST gradients, as shown in Fig. 3b. From C_{CFB} to C_{NOCFB}, meridional absolute SST gradients over the Gulf Stream and its zonal extension decrease by $3°C\ 10^{-3}\ km^{-1}$, while a dipole over the Kuroshio is characterized by a similar decrease in

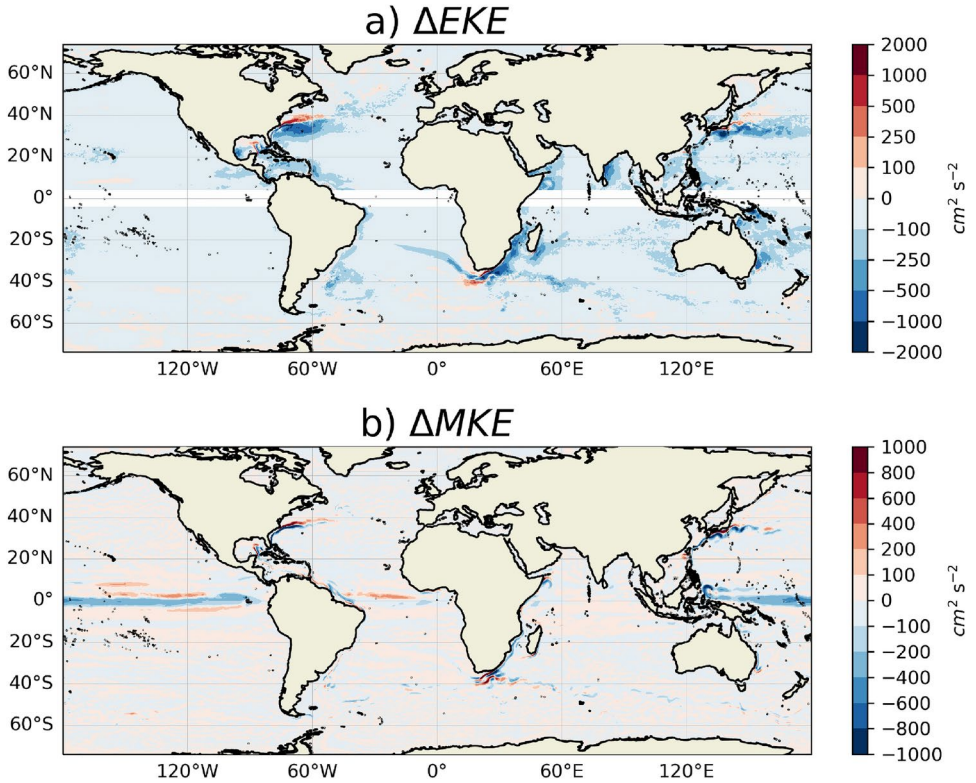

Fig. 2. The sink of kinetic energy from oceanic mesoscale eddies to the atmosphere caused by CFB induces a damping of the oceanic mesoscale activity, with a subsequent stabilization of Western Boundary Currents. (**a**) Mean surface Eddy Kinetic Energy (EKE) difference between C_{CFB} and C_{NOCFB}. (**b**) Mean surface Kinetic Energy (MKE) difference between C_{CFB} and C_{NOCFB}. The maps were generated using Python 3.0 (https://www.python.org/).

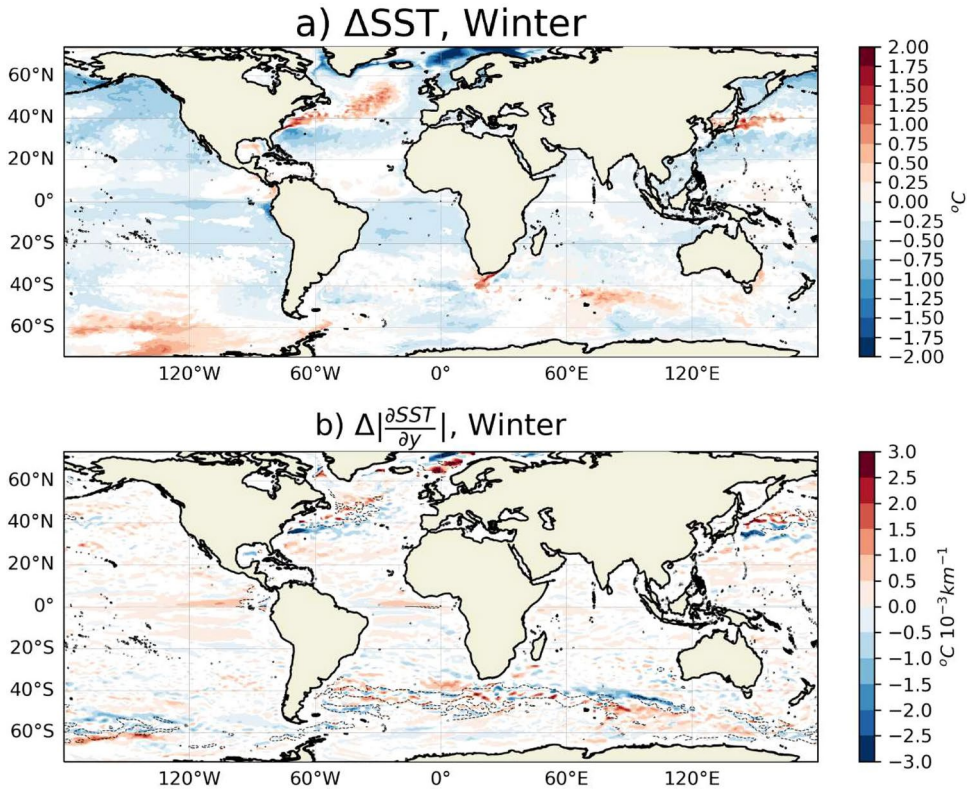

Fig. 3. Oceanic eddy killing has a rectifying effect on the SST and absolute SST meridional gradients. (**a**) Mean SST difference between C_{CFB} and C_{NOCFB}. A positive value indicates a warmer temperature in C_{CFB}. (**b**) Colors represent the difference in mean absolute meridional SST gradients between C_{CFB} and C_{NOCFB}. Black contour lines represent the mean SST gradients of C_{NOCFB} (contours of [4], $^{\circ}$C 10^{-3} km^{-1}, respectively). Only the values that have the same sign in 95% of the ensemble and that are larger than the ensemble standard deviation are shown, the remaining areas are shown in white. The coastal areas for the gradients are also masked in white due to the presence of land. The maps were generated using Python 3.0 (https://www.python.org/).

SST gradients over its path and an increase of the same order of magnitude north of its path. Over the Antarctic Circumpolar Current, which can also interact strongly with the southern extratropical storm track, SST gradients are generally reduced by up to 3°C 10^{-3} km^{-1}, except over the Agulhas Current and its zonal extension, where SST gradients are increased by 3°C 10^{-3} km^{-1}.

Over the WBCs, these differences are primarily driven by changes in mean heat transport (related to the stabilization of intensified currents paths by reducing the inverse energy cascade[62]) and, everywhere (including the WBCs), by eddy heat transport, with changes in *e.g.,* mixed layer depth being secondary drivers[57,64]. For example, in C_{NOCFB} the Gulf Stream is too meandering, causing premature separation[51,60,62]. In C_{NOCFB}, the Agulhas Current is prematurely reflected due to too large an eddy-mean flow interaction near Port Elizabeth[62]. This leads to a reduction in the mean westward advection of the mean temperature relative to that in C_{CFB}. Again, the rectification effect on the absolute meridional gradients improves the realism of the C_{NOCFB} simulation relative to C_{CFB} (see Supplemental Information).

A rectification effect on the storm track activity

WBCs are known to anchor and energize the extra-tropical storm tracks through frontal thermal air–sea interactions[17,24]. In particular, the development of cyclones is strongly dependent on baroclinic instability in the lower troposphere[18–21], which is driven by two main factors[3–5,7,8,22–24,32,44,76,77]: the large-scale meridional SST gradients that maintain meridional air temperature gradients in the lower troposphere, and the heat fluxes that can modulate them. Therefore, the upscaling effect of mesoscale CFB on SST patterns should affect both of these factors, and thus extratropical storm track activity, as we will verify hereafter. Again, we use the 1000 ensemble means derived from C_{NOCFB} to disentangle the effects of CFB from internal variability.

On the one hand, the indirect heating of the WBCs by CFB mechanically intensifies the air–sea temperature and humidity gradients, which increases the heat loss by turbulent heat fluxes by up to 80 Wm^{-2} (15%, Fig. 4a, where a positive flux indicates a transfer of heat from the ocean to the atmosphere). This should tend to increase the baroclinicity of the atmosphere[3,23,31,77] and thus act as a catalyzer for storm track activity. On the other hand, over the Gulf Stream, the weakening of the SST gradients leads to a reduction of the meridional temperature gradients in the lower atmosphere by about 1.5°C 10^{-3} km^{-1} (30% reduction, as shown in Fig. 4b). This

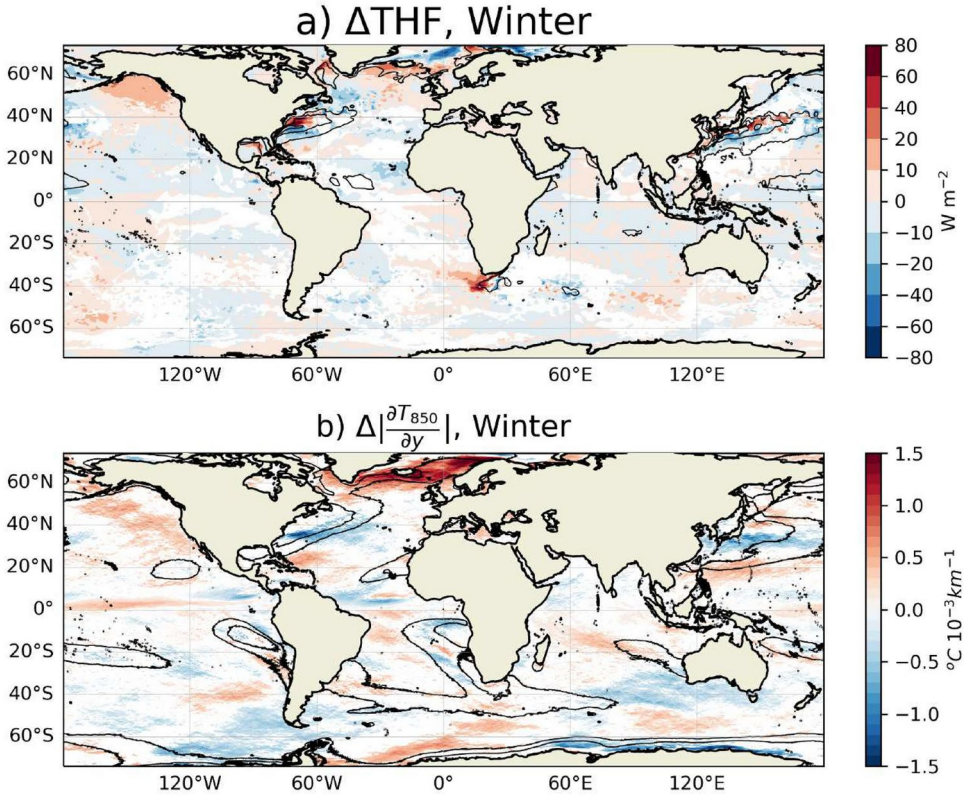

Fig. 4. The CFB-induced changes in SST drive two distinct mechanisms: an enhancement of the heat loss by turbulent heat fluxes over WBCs and a modulation of the absolute temperature meridional gradients in the lower troposphere. (**a**) The colors depict the mean turbulent heat flux difference between C_{CFB} and C_{NOCFB} while the black contour lines show the mean turbulent heat flux from C_{NOCFB} (contours of [− 400, − 300, − 200, 200, 300, 400] W km^{-1}). (**b**) The colors represent the difference in the mean absolute meridional air-temperature gradients at 850 hPa between C_{CFB} and C_{NOCFB} while the black contour lines depict the mean absolute air-temperature gradients at 850 hPa from C_{NOCFB} (contours of [7, 9] °C 10^{-3}km^{-1}, respectively). Again, to unravel the effect of CFB from the model internal variability, the mean values of heat fluxes and 850 hPa temperature absolute gradients from C_{NOCFB} and the mean values difference between C_{CFB} and C_{NOCFB} are estimated as the median of the ensemble of 1000 slices of 24 unique years (see Supplemental Information). Only the values that have the same sign in 95% of the ensemble and that are greater than the standard deviation of the ensemble are shown, the remaining areas are shown in white. The maps were generated using Python 3.0 (https://www.python.org/).

reduction should consequently decrease the available potential energy in the atmosphere, ultimately damping the storm track activity over the Gulf Stream[78]. With respect to the Kuroshio region, the changes in SST gradients lead to a consistent dipole pattern characterized by a decrease in lower atmospheric temperature gradients along the Kuroshio main path and an increase north of it. This should induce a dipole of decreasing and increasing baroclinicity and thus a change in storm track activity.

Finally, in the Southern Hemisphere, the CFB generally reduces the largest meridional temperature gradients in the lower troposphere, weakening storm track activity. A notable exception is over the Agulhas Current and its zonal extension, where, in agreement with the results of[64], temperature gradients in the lower atmosphere are enhanced, which should lead to a strengthening of the storm track. Note that the rectification effect of the eddy killing on the temperature gradients in the atmosphere and on the turbulent fluxes does not systematically reduce the biases between the simulations and the ERA5 reanalysis, but one should keep in mind that the simulations were not carefully tuned (see Supplemental Information).

To assess the rectifying effect of CFB on storm track activity, three classical metrics are now estimated: (i) the maximum Eady Growth Rate (EGR) at 850 hPa[30,64,79–83], which corresponds to a measure of baroclinic instability; (ii) the poleward eddy heat flux in the lower troposphere at 850 hPa ($|\overline{V'T'}|$)[21], which is a direct measure of storm-track activity; and (iii) the standard deviation of the 2–6 day band-pass filtered daily sea level pressure[84,85], which is another measure of storm-track activity. The poleward eddy heat flux at 850 hPa is computed as $|\overline{V'T'}|$, where the primes denote 2-8 day filtering and the overbar denotes the long-term mean. Note that we use the absolute value of the poleward heat flux, so a positive value indicates poleward transport. These metrics allow us to assess the rectifying effect of CFB on the storm track response via changes in heat fluxes and temperature gradients in the lower atmosphere.

The maximum (EGR) at 850 hPa is estimated as

$$\sigma_{BI} = 0.3098 \frac{g}{N\theta_{850}} \left| \frac{\partial \theta}{\partial y} \right| \quad (4)$$

where g is the gravitational acceleration, N is the buoyancy frequency (estimated between 850 and 700 hPa), and θ_{850} the potential temperature. The more positive the EGR, the more likely the cyclones are to develop[82] (equivalently, the EGR is the growth rate of the most unstable mode). Both simulations reproduce the main spatial pattern of the EGR during winter (JAS for the Southern Hemisphere and JFM for the Northern Hemisphere, see contours in Fig. 5a) with values greater than 0.5 day^{-1} over WBCs and their zonal extension (*e.g.,* [64,86]) and over a portion of the Antarctic Circumpolar Current.

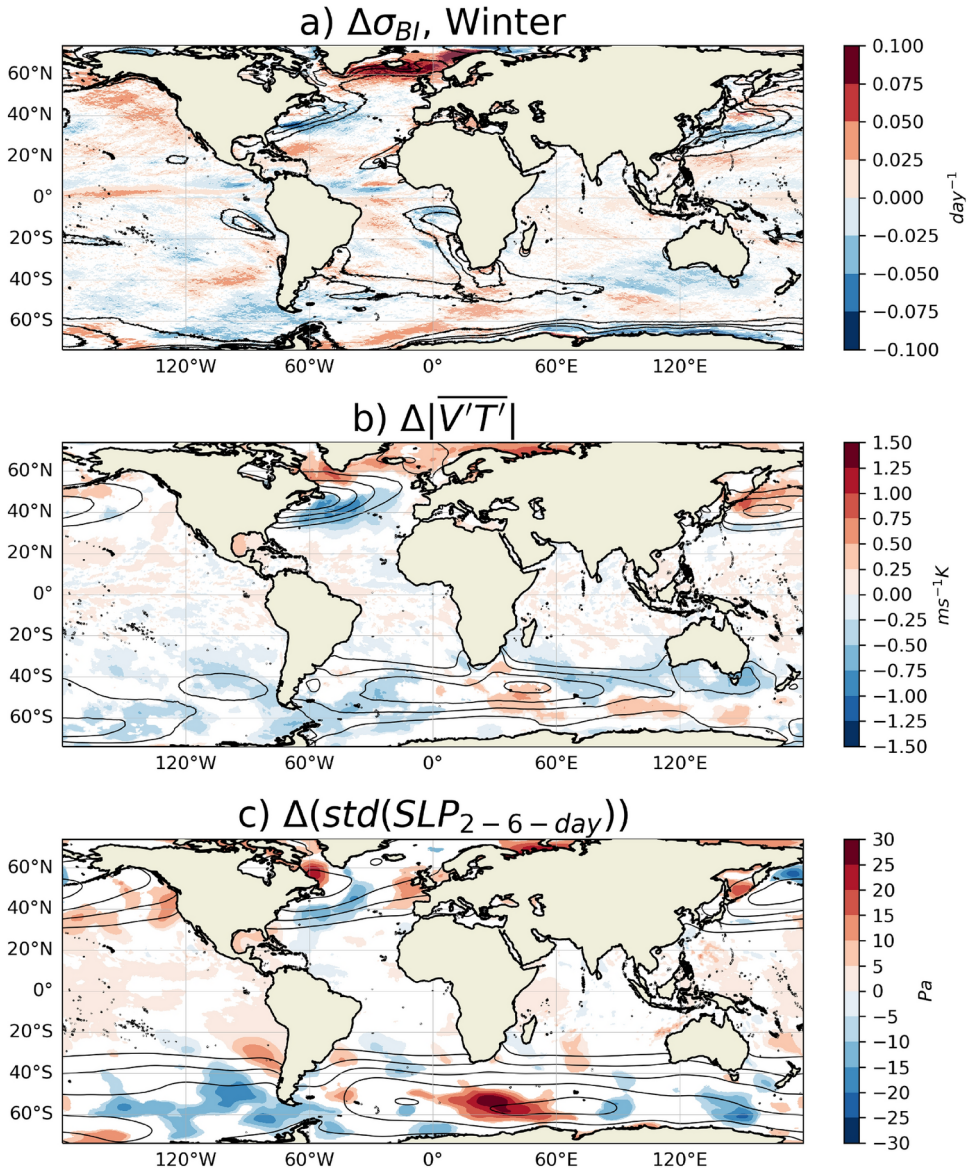

Fig. 5. The reduction of the SST-gradients modulates the storm-track activity. (**a**) The colors represent the EGR difference between C_{CFB} and C_{NOCFB} at 850 hPa during winter. The EGR contours (0.4,0.5,0.6,0.7 day^{-1}) estimated from C_{NOCFB} are also indicated. (**b**) Meridional eddy advection of heat $|\overline{V'T'}|$at 850 hPa. The colors represent $|\overline{V'T'}|$difference between C_{CFB} and C_{NOCFB}, whereas the contours depict its mean values estimated from C_{NOCFB} (one contour each 2 m s^{-1} K from 4 m s^{-1} K). (**c**) Standard deviation of the 2–6 day band-pass filtered daily sea-level pressure (in Pa). The colors represent the difference between C_{CFB} and C_{NOCFB}, the contours (one contour each 100 Pa from 200 Pa) show the values estimated from C_{NOCFB} . Only the values that have the same sign in 95% of the ensemble and that are greater than the standard deviation of the ensemble are shown, the remaining areas are shown in white. The maps were generated using Python 3.0 (https://www.python.org/).

Figure 5a shows in color the difference in EGR between C_{CFB} and the ensemble simulation of C_{NOCFB}. Across the Northern Hemisphere extratropical storm track (40–60°N), there are two regions where the EGR is significantly altered. The first is the storm track near the Gulf Stream and its zonal extension. In this region, the EGR is reduced by up to 15%. This implies the following chain of events: over this region, oceanic eddy killing weakens the meridional SST gradients by stabilizing the Gulf Stream. This in turn reduces the meridional temperature gradients in the lower troposphere, and thus the available potential energy and the baroclinicity of the lower atmosphere. This mechanism is likely to dominate over the other mechanism associated with the increase in heat loss, as suggested by the similarity of the patterns in Figs. 4b and 5a.

To confirm this hypothesis, following *e.g.,* [30,64,83], we separate the contributions of the 850 hPa temperature gradient and static stability (related to surface heat fluxes) to the change in EGR (see Fig. S3 in the Supplemental Information). It confirms that the decrease in baroclinicity from C_{NOCFB} to C_{CFB} over the Gulf Stream is mainly driven by a weakening of the temperature gradient in the lower atmosphere, which overcomes a slight increase in the effect of static stability over the Gulf Stream extension. The second region where CFB has a significant effect on EGR is, not surprisingly, the Kuroshio, where the response to CFB is significantly different from that over the Gulf Stream. Consistent with the SST and lower atmospheric temperature gradients, CFB induces a dipole characterized by a decrease in baroclinicity over the Kuroshio and an increase to the north. Again, the decomposition between the effects of static stability and temperature gradients indicates that changes in temperature gradients are the leading mechanism (Fig. S3 in the Supplemental Information).

In contrast, in the Southern Hemisphere, the effect of the CFB on extratropical storm track activity is more subtle. On the one hand, over the Antarctic Circumpolar Current, near South America and south of Australia, there is a decrease in the EGR, suggesting a weakening of the baroclinicity over these regions and thus a weaker storm track activity. On the other hand, in the vicinity of the Agulhas Current and its zonal extension, consistent with[64], oceanic eddy killing indirectly causes an increase in EGR over and south of the Agulhas Current, indicating more intense baroclinicity induced by both stronger 850 hPa temperature gradients and greater heat loss via the Agulhas Current retroflection. This is further confirmed by the decomposition of the EGR in Fig. S3 in the Supplemental Information.

In both the Northern and Southern Hemispheres, a poleward eddy flux is indicated by a positive $|\overline{V'T'}|$. Intense storm track activity is associated with large positive $|\overline{V'T'}|$values and with large values of the standard deviation of the 2–6 day band-pass filtered sea level pressure. Figure 5b shows the $|\overline{V'T'}|$difference between C_{CFB} and C_{NOCFB} (see Supplemental Information) and the contours of the largest $|\overline{V'T'}|$values estimated from C_{NOCFB}. $|\overline{V'T'}|$in both simulations has similar values to those found in the literature (*e.g.,* [4,64]) with values greater than 10 m s^{-1} K over the Gulf Stream, the Kuroshio, and the Southern Ocean (see also the evaluation of the simulations in the Supplemental Information). Consistent with the changes in EGR from C_{NOCFB} to C_{CFB}, $|\overline{V'T'}|$over the Gulf Stream is attenuated (by up to 15%), revealing a damping of storm track activity over this region. Over the Kuroshio, as expected, there is a northward shift in storm track intensity. These changes coincide with the CFB-induced modulation of SST and lower atmospheric temperature gradients. In the Southern Ocean, $|\overline{V'T'}|$is also weakened by about 10%, except in the vicinity of the Agulhas Current and its zonal extension, where CFB, by partially regulating the retroflection of the Agulhas Current, leads to a local re-energization of the storm track, in agreement with the regional study of[64].

The modulation of the storm track intensity is further confirmed by analyzing the difference in the standard deviation of the 2–6 day band-pass filtered sea level pressure between C_{CFB} and C_{NOCFB} (Fig. 5c). A similar modulation is found over the WBCs and the Antarctic Circumpolar Current, although with weaker intensity (up to 6% in the vicinity of the Agulhas Current). Note that, as mentioned above, the CFB rectification effect does not necessarily improve the realism of the simulations, since they are not tuned and biases from other mechanisms are likely.

Discussion

Overall, our results are consistent with previous studies demonstrating control of extratropical storm tracks by WBCs. Over WBCs, the more intense meridional SST gradients and intense turbulent heat fluxes are associated with baroclinic eddies that grow faster[8,23,87]. An associated shift in baroclinic wave activity results in a weaker poleward eddy heat flux. In the literature, the large meridional SST gradients and intense turbulent heat fluxes of WBCs have also been associated with the path and intensity of the storm track downstream[3,4,8,23].

Our results also provide a new perspective on how fine-scale local processes in general, and CFBs in particular, can influence climate. Using eddy-rich coupled ocean–atmosphere simulations over a long time period, with or without current feedbacks to the atmosphere, we provide evidence in a global context for the following main chain of events, which is also illustrated in Fig. 6. First, CFB causes oceanic eddy killing, *i.e.,* a damping of oceanic mesoscale activity driven by a sink of kinetic energy from mesoscale currents to the atmosphere. It subsequently reduces the eddy-mean flow interaction, stabilizing WBCs and other major currents and altering the associated advection of warm water. Especially over WBCs, oceanic eddy killing has a rectifying effect on the mean SST and its meridional gradients, modulating surface heat fluxes and temperature gradients in the lower troposphere. As a result, storm track activity is modulated in both the northern and southern hemispheres. From the oceanic point of view, the biases of the oceanic mean state (currents and SST) with respect to observations are reduced thanks to a reduction of a long-standing bias in the representation of the mean path of the western boundary currents. While this is not necessarily the case for the atmosphere, it should be noted that the global simulations have not been carefully tuned, which could lead to some compensation of biases. In addition, unlike reanalysis and observations, the simulations do not account for climate change, which may also introduce additional biases in the representation of temperature gradients and other storm track metrics.

Alternative mechanisms could possibly explain the observed modulation of the storm track from the simulation without CFB (C_{NOCFB}) to the simulation with CFB (C_{CFB}). Chaotic variability may contribute to

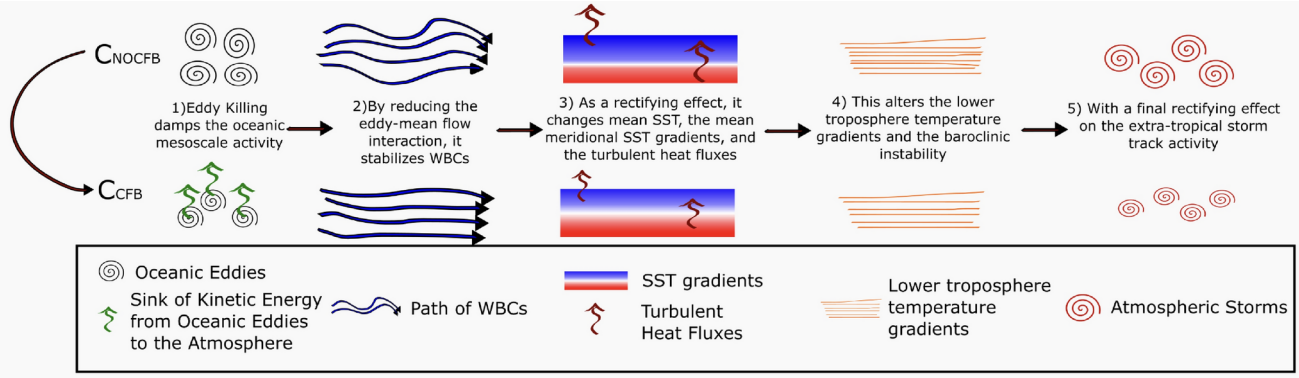

Fig. 6. Schematic representation of the chain of events induced by the mesoscale CFB.

the observed differences between these two sets of simulations. However, we have used a bootstrap method to isolate the CFB effect from it, highlighting the significant differences over WBCs. To disentangle the local CFB effect over WBCs from that in other regions, another set of simulations could also have considered CFB only over WBCs, allowing the oceanic eddy killing effect to be considered only over WBCs; this type of methodology could be applied to future studies. CFB also slightly affects SST in the Pacific equatorial region, which could potentially lead to changes in teleconnections between the Pacific equatorial region and the jet stream. However, the changes in SST are weaker than 0.5°C, which is probably too weak to influence teleconnections between *e.g.,* ENSO and the extra-tropical storm tracks[88]. There are also significant differences along the sea ice margins that could affect the polar frontal jet and thus storm genesis, but they are further north than the observed changes over WBCs. While a global approach has the advantage of allowing local effects to propagate into the far-field and then have a rectifying effect on the large-scale, a regional approach has a higher degree of constraint on model-internal variability and is less affected by global model bias. Numerous regional studies have consistently demonstrated a reduction of the EKE (*e.g.,* [51,54–56,59,63]) and the resulting rectification of the WBCs[57,60,62].

The indirect effects of CFB on SST highlighted in this study are consistent with the regional results of[57] and[64] for the Agulhas Current, and are also found in other simulations such as those of[58]. Furthermore, the changes in EGR and $|\overline{V'T'}|$across the Agulhas Current are consistent with the results of[64], which performed regionally coupled simulations that are per se unaffected by remote changes caused by CFB. Finally, to further strengthen the robustness of our conclusions, we carried out a pair of regional atmospheric simulations over the Gulf Stream for a period of 5 years, differing only in their SST forcing: WRF_{CFB} is forced by the SST of C_{CFB} , and WRF_{NOCFB} is forced by the SST of C_{NOCFB} (see Supplemental Information). These simulations are by construction largely constrained by their open boundary conditions (see Supplemental Information). From WRF_{NOCFB} to WRF_{CFB}, a weakening of $|\overline{V'T'}|$is also observed as a rectifying effect of the CFB, providing additional support for the validity of our results from the global coupled simulations.

The importance of fine-scale ocean–atmosphere interactions in determining climate changes the classical view of the atmosphere as a large-scale forcing on the ocean, initiating a turbulent cascade of energy. At the fine scale, the ocean interacts with the atmosphere, altering the entire energy cascade in the ocean. These results also shed light on possible sources of bias in climate models. As suggested by[64], the CFB and the ocean thermal feedback are inextricably linked and can act together to shape the climate. Both represent physical processes and should not be considered as adjustment variables in modeling. Global climate models should therefore take them into account, especially if they are tuned to fit observations (which was not the case in our simulations). This would improve both climate projections and short-term forecasts.

Other regions may also be affected by the CFB upscaling effect. For example, the equatorial region is under the influence of both the oceanic eddy killing and the large-scale slowing of the mean currents by the CFB (see Fig. 2). The associated changes in meridional SST gradients may affect the overlying atmosphere and the Intertropical Convergence Zone. This will be the focus of future research. There are still large uncertainties in the current satellite observations that do not allow coherent observations of surface stress and currents[52]. Estimates of coupling coefficients, wind work, oceanic mesoscale activity, and related eddy-mean-flow interactions thus suffer from large uncertainties[47,52,89]. Future satellite projects such as Odysea[90,91] aim to coherently measure total surface currents and surface stress. This would greatly contribute to a better understanding of the air-sea exchange of momentum and heat, as well as the cascade of energy in the interior ocean. In addition, such observations would allow to better validate and constrain coupled ocean-atmosphere models.

Methods

Models

The following description of the models is derived from[45] with very few modifications. EC-Earth3 is a global coupled climate model[68,69] that is used in a wide range of studies from paleoresearch to climate projections, including seasonal and decadal predictions. The atmospheric component of EC-Earth is the Integrated Forecast System (IFS) and uses a reduced Gaussian grid with 91 vertical levels. The horizontal domain is based on a spectral truncation at T1279 (corresponding to a nominal spatial resolution of $\approx$ 15 km near the equator). The

H-TESSEL model is used for the land surface and is an integral part of the IFS atmospheric model (see[92] for details). The ECMWF bulk formulas are used over the ocean (see the IFS ECMWF Manual Part IV and[93] for a description). The ocean component is the Nucleus for European Modelling of the Ocean (NEMO,[94]) version 3.6. It is based on the ORCA12 configuration, which uses a tripolar grid with poles over northern North America, Siberia, and Antarctica with a resolution of about $\frac{1}{12}$ °and 75 vertical levels. NEMO includes the Louvain la Neuve sea ice model version 3 (LIM3,[95]), a dynamic thermodynamic sea ice model with 5 ice thickness categories. The atmosphere/land and ocean/sea ice components are coupled by the OASIS-MCT (Ocean, Atmosphere, Sea Ice, Soil) coupler[96] at hourly resolution. Both spatial resolutions meet the requirements to properly simulate the extra-tropical storm tracks, as shown in[23]. Note that the PRIMAVERA project intended to focus on model sensitivity to numerical resolution, so the simulations were not carefully designed and tuned to maximize realism.

Experiments

Two global coupled simulations are performed over a period of 80 years (C_{NOCFB}) and 24 years (C_{CFB}). The simulations differ only in the degree of coupling considered. C_{NOCFB} uses the absolute wind to estimate the surface stress (Eq. 2), thus ignoring CFB (see[45]), while C_{CFB} uses the relative wind (Eq. 1) in both the atmospheric boundary layer scheme and the surface layer scheme according to[45]. Note that CFB is disabled over the ice. The two simulations start from the same restart after a 10-year spin-up, using the C_{NOCFB} configuration from an ocean at rest and keeping the greenhouse gas forcing constant (following the HighResMIP protocol defined in[68] for the control simulation), and thus do not account for climate change.

The PRIMAVERA simulations are evaluated against the observations in[71], showing good agreement with the observations and an overall improvement in the realism of the simulations compared to simulations with coarser spatial resolution. We also provide an additional evaluation of the simulations in the Supplemental Information. In summary, the simulations show good agreement with the observations in the representation of the mean oceanic and atmospheric large-scale and mesoscale circulations and mean states. In particular, the dynamics of the WBCs and their mean paths are well represented, especially in the C_{CFB} simulation. This is also reflected in the weak biases in SST and air temperature over the WBCs. Finally, in agreement with[71], the atmospheric extra-tropical storm tracks are also well represented.

Spatial filter

Following[47] and[58], we use a spatial Gaussian filter to isolate oceanic mesoscale anomalies from the large-scale signal with $sigma = 12$. The Gaussian weights of points located at distances greater than 3σ are considered to be zero. Thus, the Gaussian filter is applied only to a window $(6\sigma + 1) \times (6\sigma + 1)$. Following the mathematical properties of the Gaussian filter, we can define an analytical expression for the cutoff spatial frequency (wavenumber): $\nu_c = \sqrt{\ln(c)}/(2\pi.\sigma.d_x)$ Where $1/c$ is the cutoff (the Gaussian filter response is divided by c in the power response), d_x is the spatial resolution in km, and ν_c is the cutoff wavenumber in km^{-1}. The resulting filter has a cutoff of ≈ 300 km.

Coupling coefficient

As in[47], s_τ is defined as the slope of the regression between surface stress curl and ocean current vorticity. It is evaluated at each grid point for both simulations and observations. The fields are first temporally averaged using a 29-days running mean to suppress weather-related variability[37], and the large-scale signal is removed using the high-pass Gaussian spatial filter described above.

Estimation of the uncertainties

To estimate the uncertainties due to the chaotic variability of the coupled simulations, and thus to disentangle the differences due to CFB from the internal variability, we used a bootstrap method[72]. Our population data are the 80 years of a given variable of the C_{NOCFB} simulation. We have implemented the following main steps:

- Replace the population data with a sample of 24 unique (not necessarily consecutive) random years from the 80-year period of C_{NOCFB}. Depending on the analysis, we will consider the winter period (average over January–February–March for the Northern Hemisphere, July–August–September for the Southern Hemisphere) or the average over the entire year.
- Sample with replacement 1000 times, allowing us to compute an ensemble of 1000 different C_{NOCFB} means and mean differences between C_{CFB} and C_{NOCFB}.
- Obtain the difference between C_{NOCFB} samples (1000) and C_{CFB}.
- Estimate the mean of each sample and its mean difference with C_{CFB}.
- Estimate the median of the sample means and mean differences.To better assess the error associated with a given variable, we estimated the median and standard deviation by considering the 95% confidence interval, i.e., by considering data from the 2.5 percentile to the 97.5 percentile. Note that using the mean instead of the median does not change the results. To ensure a robust representation of the consistent signal caused by CFB, we then focused on values where at least 95% of the sample means have the same sign and are greater than the standard deviation of the ensemble. By using this approach, we effectively quantified the uncertainties associated with our estimates of the CFB effect on the extra-tropical storm track, while also accounting for the internal variability within the C_{NOCFB} simulation.

Data availability

The EC-Earth climate model code is hosted on the EC-Earth development portal (https://dev.ec-earth.org/login) under an svn repository that requires an account. Only staff of institutes that are part of the EC-Earth consortium can get an account, mainly due to the IFS code license of ECMWF. Requests for specific data can be sent to L. Renault (lionel.renault@ird.fr).

Received: 30 July 2024; Accepted: 9 December 2024
Published online: 30 December 2024

References

1. Talley, L. D., Reid, J. L. & Robbins, P. E. Data-based meridional overturning streamfunctions for the global ocean. *J. Clim.* **16**, 3213–3226 (2003).
2. Kuwano-Yoshida, A. & Minobe, S. Storm-track response to SST fronts in the northwestern pacific region in an AGCM. *J. Clim.* **30**, 1081–1102 (2017).
3. Czaja, A., Frankignoul, C., Minobe, S. & Vannière, B. Simulating the midlatitude atmospheric circulation: What might we gain from high-resolution modeling of air–sea interactions?. *Curr. Clim. Change Rep.* **5**, 390–406 (2019).
4. Nakamura, H., Sampe, T., Tanimoto, Y. & Shimpo, A. The Ocean–Atmosphere Interaction. Observed associations among storm tracks, jet streams and midlatitude oceanic fronts. Earth's Climate. *Geophys. Monogr.* **147**, 329–345 (2004).
5. Minobe, S., Kuwano-Yoshida, A., Komori, N., Xie, S.-P. & Small, R. J. Influence of the Gulf Stream on the troposphere. *Nature* **452**, 206–209 (2008).
6. Shaw, T. et al. Storm track processes and the opposing influences of climate change. *Nat. Geosci.* **9**, 656–664 (2016).
7. Tsopouridis, L., Spengler, T. & Spensberger, C. Smoother versus sharper gulf stream and kuroshio sea surface temperature fronts: effects on cyclones and climatology. *Weather Clim. Dyn.* **2**, 953–970 (2021).
8. Bui, H. & Spengler, T. On the influence of sea surface temperature distributions on the development of extratropical cyclones. *J. Atmos. Sci.* **78**, 1173–1188 (2021).
9. Trenberth, K. E. & Stepaniak, D. P. Seamless poleward atmospheric energy transports and implications for the hadley circulation. *J. Clim.* **16**, 3706–3722 (2003).
10. Chang, E. K., Lee, S. & Swanson, K. L. Storm track dynamics. *J. Clim.* **15**, 2163–2183 (2002).
11. Raible, C. & Blender, R. Northern hemisphere midlatitude cyclone variability in GCM simulations with different ocean representations. *Clim. Dyn.* **22**, 239–248 (2004).
12. Hamlet, A. F., Mote, P. W., Clark, M. P. & Lettenmaier, D. P. Effects of temperature and precipitation variability on snowpack trends in the western united states. *J. Clim.* **18**, 4545–4561 (2005).
13. Shepherd, T. G. Atmospheric circulation as a source of uncertainty in climate change projections. *Nat. Geosci.* **7**, 703–708 (2014).
14. Priestley, M. D. et al. An overview of the extratropical storm tracks in cmip6 historical simulations. *J. Clim.* **33**, 6315–6343 (2020).
15. Priestley, M. D., Ackerley, D., Catto, J. L. & Hodges, K. I. Drivers of biases in the cmip6 extratropical storm tracks. Part i: Northern hemisphere. *J. Clim.***36**, 1451–1467 (2023).
16. Brayshaw, D. J., Hoskins, B. & Blackburn, M. The basic ingredients of the north atlantic storm track. part i. Land-sea contrast and orography. *J. Atmos. Sci.* **66**, 2539–2558 (2009).
17. Brayshaw, D. J., Hoskins, B. & Blackburn, M. The basic ingredients of the north atlantic storm track. part ii. Sea surface temperatures. *J. Atmos. Sci.* **68**, 1784–1805 (2011).
18. Holton, J. R. et al. Stratosphere–troposphere exchange. *Rev. Geophys.* **33**, 403–439 (1995).
19. Grotjahn, R. Baroclinic instability. Encyclopedia of. *Atmos. Sci.* **419**, 467 (2003).
20. Hoskins, B. J. & Valdes, P. J. On the existence of storm-tracks. *J. Atmos. Sci.* **47**, 1854–1864 (1990).
21. Nakamura, H. & Shimpo, A. Seasonal variations in the southern hemisphere storm tracks and jet streams as revealed in a reanalysis dataset. *J. Clim.* **17**, 1828–1844 (2004).
22. ONeill, L. W., Haack, T., Chelton, D. B. & Skyllingstad, E. The gulf stream convergence zone in the time-mean winds. *J. Atmos. Sci.* **74**, 2383–2412 (2017).
23. Small, R. J., Msadek, R., Kwon, Y.-O., Booth, J. F. & Zarzycki, C. Atmosphere surface storm track response to resolved ocean mesoscale in two sets of global climate model experiments. *Clim. Dyn.* **52**, 2067–2089 (2019).
24. Seo, H. et al. Ocean mesoscale and frontal-scale ocean–atmosphere interactions and influence on large-scale climate: A review. *J. Clim.* **36**, 1981–2013 (2023).
25. Nakamura, H., Sampe, T., Goto, A., Ohfuchi, W. & Xie, S.-P. On the importance of midlatitude oceanic frontal zones for the mean state and dominant variability in the tropospheric circulation. *Geophys. Res. Lett.* **35** (2008).
26. Nonaka, M. et al. Air–sea heat exchanges characteristic of a prominent midlatitude oceanic front in the south Indian ocean as simulated in a high-resolution coupled GCM. *J. Clim.* **22**, 6515–6535 (2009).
27. Hotta, D. & Nakamura, H. On the significance of the sensible heat supply from the ocean in the maintenance of the mean baroclinicity along storm tracks. *J. Clim.* **24**, 3377–3401 (2011).
28. Josey, S. A., Kent, E. C. & Taylor, P. K. New insights into the ocean heat budget closure problem from analysis of the soc air–sea flux climatology. *J. Clim.* **12**, 2856–2880 (1999).
29. Kwon, Y.-O. et al. Role of the gulf stream and Kuroshio-Oyashio systems in large-scale atmosphere–ocean interaction: A review. *J. Clim.* **23**, 3249–3281 (2010).
30. Small, R. J., Tomas, R. A. & Bryan, F. O. Storm track response to ocean fronts in a global high-resolution climate model. *Clim. Dyn.* **43**, 805–828 (2014).
31. Haualand, K. F. & Spengler, T. Relative importance of tropopause structure and diabatic heating for baroclinic instability. *Weather Clim. Dyn.* **2**, 695–712 (2021).
32. Reeder, M. J., Spengler, T. & Spensberger, C. The effect of sea surface temperature fronts on atmospheric frontogenesis. *J. Atmos. Sci.* **78**, 1753–1771 (2021).
33. Jensen, T. G., Campbell, T. J., Allard, R. A., Small, R. J. & Smith, T. A. Turbulent heat fluxes during an intense cold-air outbreak over the kuroshio extension region: Results from a high-resolution coupled atmosphere-ocean model. *Ocean Dyn.* **61**, 657–674 (2011).
34. Grossman, R. L. & Betts, A. K. Air-sea interaction during an extreme cold air outbreak from the eastern coast of the united states. *Mon. Weather Rev.* **118**, 324–342 (1990).
35. Xue, H., Bane, J. M. & Goodman, L. M. Modification of the gulf stream through strong air–sea interactions in winter: Observations and numerical simulations. *J. Phys. Oceanogr.* **25**, 533–557 (1995).
36. Stammer, D. Global characteristics of ocean variability estimated from regional topex/poseidon altimeter measurements. *J. Phys. Oceanogr.* **27**, 1743–1769 (1997).
37. Chelton, D. B., Schlax, M. G. & Samelson, R. M. Summertime coupling between sea surface temperature and wind stress in the California current system. *J. Phys. Oceanogr.* **37**, 495–517 (2007).
38. Small, R. et al. Air–sea interaction over ocean fronts and eddies. *Dyn. Atm. Oceans* **45**, 274–319 (2008).

39. Large, W. & Yeager, S. On the observed trends and changes in global sea surface temperature and air–sea heat fluxes (1984–2006). *J. Clim.* **25**, 6123–6135 (2012).
40. Moreton, S., Ferreira, D., Roberts, M. & Hewitt, H. Air-sea turbulent heat flux feedback over mesoscale eddies. *Geophys. Res. Lett.* **48**, e2021GL095407 (2021).
41. Holmes, R. M., Renault, L., Maillard, L. & Boucharel, J. Air–sea coupling feedbacks over tropical instability waves. *J. Phys. Oceanogr.* (2024).
42. Bishop, S. P., Small, R. J. & Bryan, F. O. The global sink of available potential energy by mesoscale air–sea interaction. *J. Adv. Model. Earth Syst.* **12**, e2020MS002118 (2020).
43. Renault, L., Masson, S., Oerder, V., Colas, F. & McWilliams, J. Modulation of the oceanic mesoscale activity by the mesoscale thermal feedback to the atmosphere. *J. Phys. Oceanogr.* **53**, 1651–1667 (2023).
44. Foussard, A., Lapeyre, G. & Plougonven, R. Storm track response to oceanic eddies in idealized atmospheric simulations. *J. Clim.* **32**, 445–463 (2019).
45. Renault, L., Lemarié, F. & Arsouze, T. On the implementation and consequences of the oceanic currents feedback in ocean-atmosphere coupled models. *Ocean Model.* **141**, 101423 (2019).
46. Bye, J. A. Large-scale momentum exchange in the coupled atmosphere–ocean. *Elsevier Oceanogr. Ser.* **40**, 51–61 (1985).
47. Renault, L., Masson, S., Oerder, V., Jullien, S. & Colas, F. Disentangling the mesoscale ocean–atmosphere interactions. *J. Geophys. Res. Oceans* **124**, 2164–2178 (2019).
48. Pacanowski, R. Effect of equatorial currents on surface stress. *J. Phys. Oceanogr.* **17**, 833–838 (1987).
49. Luo, J.-J., Masson, S., Roeckner, E., Madec, G. & Yamagata, T. Reducing climatology bias in an ocean–atmosphere CGCM with improved coupling physics. *J. Clim.* **18**, 2344–2360 (2005).
50. Scott, R. B. & Xu, Y. An update on the wind power input to the surface geostrophic flow of the world ocean. *Deep Sea Res. Part I* **56**, 295–304 (2009).
51. Renault, L., Molemaker, M. J., Gula, J., Masson, S. & McWilliams, J. C. Control and stabilization of the gulf stream by oceanic current interaction with the atmosphere. *J. Phys. Oceanogr.* **46**, 3439–3453 (2016).
52. Renault, L., McWilliams, J. C. & Masson, S. Satellite observations of imprint of oceanic current on wind stress by air–sea coupling. *Sci. Rep.* **7**, 17747 (2017).
53. Xu, C., Zhai, X. & Shang, X.-D. Work done by atmospheric winds on mesoscale ocean eddies. *Geophys. Res. Lett.* **43** (2016).
54. Renault, L. et al. Modulation of wind work by oceanic current interaction with the atmosphere. *J. Phys. Oceanogr.* **46**, 1685–1704 (2016).
55. Seo, H., Miller, A. J. & Norris, J. R. Eddy-wind interaction in the California current system: Dynamics and impacts. *J. Phys. Oceanogr.* **46**, 439–459 (2016).
56. Oerder, V., Colas, F., Echevin, V., Masson, S. & Lemarié, F. Impacts of the mesoscale ocean-atmosphere coupling on the Peru-Chile ocean dynamics: The current-induced wind stress modulation. *J. Geophys. Res. Oceans* (2018).
57. Renault, L., McWilliams, J. C. & Penven, P. Modulation of the agulhas current retroflection and leakage by oceanic current interaction with the atmosphere in coupled simulations. *J. Phys. Oceanogr.* **47**, 2077–2100 (2017).
58. Renault, L., Masson, S., Arsouze, T., Madec, G. & McWilliams, J. C. Recipes for how to force oceanic model dynamics. *J. Adv. Model. Earth Syst.***12**, e2019MS001715 (2020).
59. Jullien, S. et al. Impact of ocean-atmosphere current feedback on ocean mesoscale activity: Regional variations and sensitivity to model resolution. *J. Clim.* **33**, 2585–2602 (2020).
60. Renault, L., Marchesiello, P. & Contreras, M. Coaction of top and bottom drags in gulf stream dynamics. *J. Geophys. Res. Oceans* **128**, e2022JC018939 (2023).
61. Seo, H. Distinct influence of air–sea interactions mediated by mesoscale sea surface temperature and surface current in the arabian sea. *J. Clim.* **30**, 8061–8080 (2017).
62. Renault, L., Marchesiello, P., Masson, S. & McWilliams, J. C. Remarkable control of western boundary currents by eddy killing, a mechanical air–sea coupling process. *Geophys. Res. Lett.* **46**, 2743–2751 (2019).
63. Song, H., Marshall, J., McGillicuddy Jr, D. J. & Seo, H. Impact of current-wind interaction on vertical processes in the southern ocean. *J. Geophys. Res. Oceans* **125**, e2020JC016046 (2020).
64. Seo, H., Song, H., O'Neill, L. W., Mazloff, M. R. & Cornuelle, B. D. Impacts of ocean currents on the south Indian ocean extratropical storm track through the relative wind effect. *J. Clim.* **34**, 9093–9113 (2021).
65. Contreras, M., Renault, L. & Marchesiello, P. Understanding energy pathways in the gulf stream. *J. Phys. Oceanogr.* (2022).
66. Larrañaga, M., Renault, L. & Jouanno, J. Partial control of the gulf of Mexico dynamics by the current feedback to the atmosphere. *J. Phys. Oceanogr.* **52**, 2515–2530 (2022).
67. Renault, L., McWilliams, J. C. & Penven, P. Modulation of the agulhas current retroflection and leakage by oceanic current interaction with the atmosphere in coupled simulations. *J. Phys. Oceanogr.* **47**, 2077–2100 (2017).
68. Haarsma, R. J. *et al.* High resolution model intercomparison project (highresmip v1. 0) for cmip6. *Geosci. Model Dev.* **9**, 4185–4208 (2016).
69. Döscher, R. et al. The ec-earth3 earth system model for the coupled model intercomparison project 6. *Geosci. Model Dev.* **15**, 2973–3020 (2022).
70. Haarsma, R. et al. Highresmip versions of ec-earth: Ec-earth3p and ec-earth3p-hr - description, model computational performance and basic validation. *Geosci. Model Dev.* **13**, 3507–3527. https://doi.org/10.5194/gmd-13-3507-2020 (2020).
71. Moreno-Chamarro, E. et al. The very-high resolution configuration of the ec-earth global model for highresmip. *Geosci. Model Dev. Discuss.* **1–49**, 2024. https://doi.org/10.5194/gmd-2024-119 (2024).
72. Efron, B. & Tibshirani, R. J. *An Introduction to the Bootstrap* (CRC Press, 1994).
73. Rai, S., Hecht, M., Maltrud, M. & Aluie, H. Scale of oceanic eddy killing by wind from global satellite observations. *Sci. Adv.***7**, eabf4920 (2021).
74. Fu, L.-L. & Qiu, B. Low-frequency variability of the north pacific ocean: The roles of boundary-and wind-driven baroclinic rossby waves. *J. Geophys. Res. Oceans* **107** (2002).
75. Renault, L., Arsouze, T. & Ballabrera-Poy, J. On the influence of the current feedback to the atmosphere on the western mediterranean sea dynamics. *J. Geophys. Res. Oceans* **126**, e2020JC016664 (2021).
76. Czaja, A. & Blunt, N. A new mechanism for ocean–atmosphere coupling in midlatitudes. *Q. J. R. Meteorol. Soc.* **137**, 1095–1101 (2011).
77. Ogawa, F. & Spengler, T. Influence of mid-latitude sea surface temperature fronts on the atmospheric water cycle and storm track activity. *Weather Clim. Dyn.* **5**, 1031–1042 (2024).
78. Grotjahn, R. *Dynamical meteorology|Baroclinic Instability* (Elsevier, 2015).
79. Charney, J. G. The dynamics of long waves in a baroclinic westerly current. *J. Atmos. Sci.* **4**, 136–162 (1947).
80. Eady, E. T. Long waves and cyclone waves. *Tellus* **1**, 33–52 (1949).
81. Lindzen, R. & Farrell, B. A simple approximate result for the maximum growth rate of baroclinic instabilities. *J. Atmos. Sci.* **37**, 1648–1654 (1980).
82. Vallis, G. Atmospheric and oceanic fluid dynamics: fundamentals and large-scale circulation, 2006 (2006).
83. Yin, J. H. A consistent poleward shift of the storm tracks in simulations of 21st century climate. *Geophys. Res. Lett.* **32** (2005).
84. Ulbrich, U., Leckebusch, G. C. & Pinto, J. G. Extra-tropical cyclones in the present and future climate: a review. *Theoret. Appl. Climatol.* **96**, 117–131 (2009).

85. Brayshaw, D. J., Woollings, T. & Vellinga, M. Tropical and extratropical responses of the north Atlantic atmospheric circulation to a sustained weakening of the moc. *J. Clim.* **22**, 3146–3155 (2009).
86. Ma, X. et al. Importance of resolving Kuroshio front and eddy influence in simulating the north pacific storm track. *J. Clim.* **30**, 1861–1880 (2017).
87. O'Reilly, C. H. & Czaja, A. The response of the pacific storm track and atmospheric circulation to Kuroshio extension variability. *Q. J. R. Meteorol. Soc.* **141**, 52–66 (2015).
88. Trascasa-Castro, P., Maycock, A. C., Yiu, Y. Y. S. & Fletcher, J. K. On the linearity of the stratospheric and euro-Atlantic sector response to ENSO. *J. Clim.* **32**, 6607–6626 (2019).
89. Arbic, B. K., Polzin, K. L., Scott, R. B., Richman, J. G. & Shriver, J. F. On eddy viscosity, energy cascades, and the horizontal resolution of gridded satellite altimeter products. *J. Phys. Oceanogr.* **43**, 283–300 (2013).
90. Bourassa, M. A., Rodriguez, E. & Chelton, D. Winds and currents mission: Ability to observe mesoscale air/sea coupling. In *Geoscience and Remote Sensing Symposium (IGARSS), 2016 IEEE International*, 7392–7395 (IEEE, 2016).
91. Rodríguez, E. et al. Estimating ocean vector winds and currents using a ka-band pencil-beam doppler scatterometer. *Remote Sens.* **10**, 576 (2018).
92. Hazeleger, W. et al. Ec-earth: a seamless earth-system prediction approach in action. *Bull. Am. Meteorol. Soc.* **91**, 1357–1364 (2010).
93. Bonino, G., Iovino, D., Brodeau, L. & Masina, S. The bulk parameterizations of turbulent air-sea fluxes in nemo4: the origin of sea surface temperature differences in a global model study. *Geosci. Model Dev.* **15**, 6873–6889 (2022).
94. Madec, G. *et al.* Nemo ocean engine. *None* (2015).
95. Vancoppenolle, M. et al. *The louvain-la-neuve sea ice model* (Notes du pole de modélisation, Institut Pierre-Simon Laplace (IPSL), 2012).
96. Craig, A., Valcke, S. & Coquart, L. Development and performance of a new version of the oasis coupler, oasis3-mct_3. 0. *Geosci. Model Dev.* **10**, 3297–3308 (2017).

Author contributions

L.R. conceived the study, L.R. and T.A. conceived the experiments, T.A. conducted the experiments. All authors analyzed the results and reviewed the manuscript.

Declarations

Competing interests

The authors declare no competing interests.

Additional information

Supplementary Information The online version contains supplementary material available at https://doi.org/10.1038/s41598-024-82667-2.

Correspondence and requests for materials should be addressed to L.R.

Reprints and permissions information is available at www.nature.com/reprints.

Publisher's note Springer Nature remains neutral with regard to jurisdictional claims in published maps and institutional affiliations.